Hindawi
Advances in Civil Engineering
Volume 2024, Article ID 4561737, 18 pages
https://doi.org/10.1155/2024/4561737

Research Article

Eccentric Compression Performance of Core-Steel Tube with T-Shaped Steel Reinforced Concrete Column

Liang Gao,[1] Peng Wang,[2] and Xuehui You [2]

[1]*School of Management Engineering, Shandong Jianzhu University, Jinan 250101, China*
[2]*School of Civil Engineering, Xi'an University of Architecture and Technology, Xi'an 710055, China*

Correspondence should be addressed to Xuehui You; youxuehui4242@163.com

Received 13 October 2023; Revised 24 March 2024; Accepted 5 April 2024; Published 26 April 2024

Academic Editor: André Martins

This paper introduces a novel steel–concrete composite column referred to as the core-steel tube with T-shaped steel reinforced concrete (CSTRC) column, which is composed of a core steel tube with T-shaped steel embedded in a reinforced concrete column. To investigate the mechanical performance of the CSTRC column under eccentric compressive load, the load–deformation response, stress, and strain distribution of CSTRC columns under eccentric load are analyzed by finite element software. Furthermore, the effects of slenderness ratio, concrete and steel strength on the eccentric compression performance of CSTRC columns are also discussed. Finally, a set of formulas for predicting the ultimate strength of the CSTRC columns is proposed. The study results reveal that: (1) The established finite element model accurately predicts bearing capacity and strain development. (2) When the eccentricity is 0.2, the specimen exhibits characteristics indicative of small eccentricity failure. Conversely, when the eccentricity is 0.8, the specimen demonstrates traits associated with large eccentricity failure. Furthermore, as the eccentricity increases, there is a notable decrease in the bearing capacity of the specimen. (3) The slenderness ratio affects the failure mode of the CSTRC columns, with consideration for second-order effects necessary when the ratio exceeds 22. (4) Increasing the concrete strength, steel strength, and steel ratio significantly enhances the ultimate load values of the CSTRC columns. (5) A comparison between calculated and simulated values demonstrates good agreement, validating the accuracy of the proposed method.

1. Introduction

Due to the excellent mechanical properties and high bearing capacity, concrete-filled steel tubular (CFST) columns have found widespread application in engineering construction [1–3]. In recent decades, researchers have extensively investigated their mechanical performance, including axial compression behavior [4–6], eccentric compression behavior [7–9], and seismic behavior [10–12]. As a result, the design and construction methods for CFST columns have been refined and enhanced. Nevertheless, CFST columns have many problems, including intricate joint connections, limited fire resistance, and susceptibility to local buckling. Moreover, exposure to harsh environmental conditions can lead to rusting of the steel tube in CFST columns, potentially compromising their service life [13, 14].

As an alternative solution, scholars have introduced a novel steel-concrete composite column known as the concrete-filled core-steel tube (CFCST) column. Distinguishing itself from CFST columns, the steel tube in the CFCST column is embedded within a reinforced concrete column. Figure 1 depicts three distinctive cross-sections of the CFCST column. As evident, the steel tube is embedded within the concrete, mitigating its vulnerability to corrosion and markedly improving the overall fire resistance performance of the columns. Presently, CFCST columns have been successfully employed in numerous high-rise buildings in China [15–18].

In recent years, CFCST columns have garnered considerable attention. Scholars have conducted extensive research on the mechanical performance and design methodologies associated with CFCST columns. This includes investigations into axial compression performance, seismic behavior, and bending performance. Kang et al. [19] and Nie et al. [20] studied the axial compression performance of the CFCST columns experimentally. Qian et al. [21] and Ji et al. [22] studied the seismic performance of the CFCST columns. All

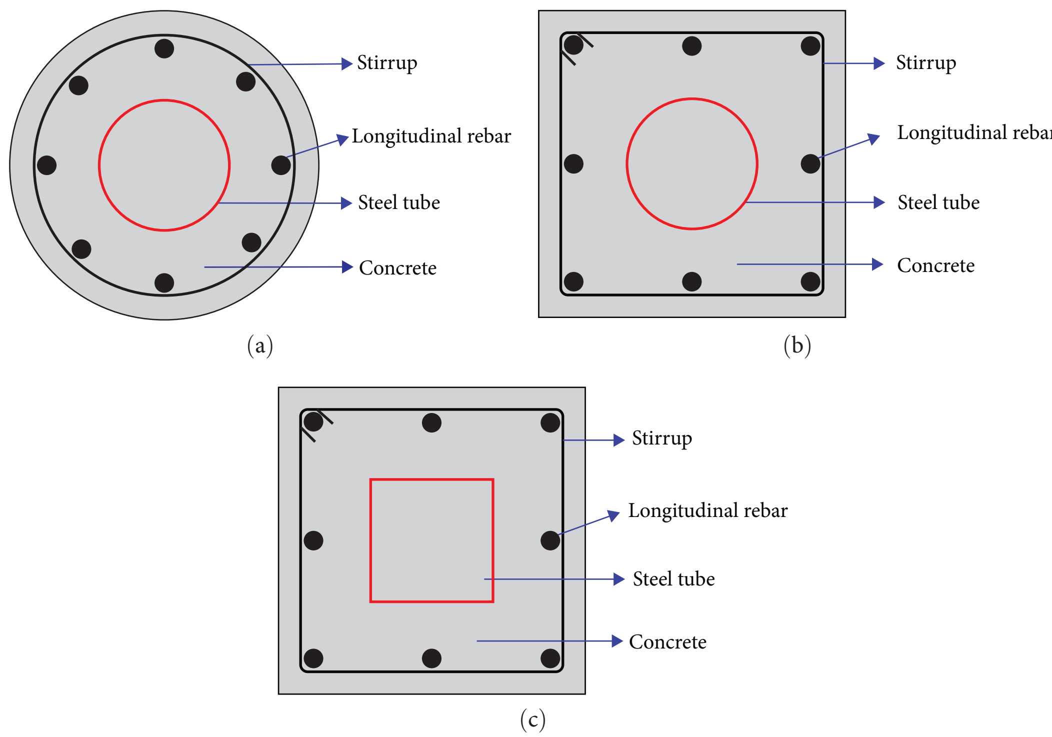

Figure 1: Typical cross-section of the CFCST columns: (a) circular reinforced concrete with circular steel tube; (b) square reinforced concrete with circular steel tube; (c) square reinforced concrete with square steel tube.

results show that CFCST columns have good bearing capacity. However, further research indicates noticeable distinctions in the mechanical performance between the concrete core and the outer concrete of CFCST columns. When subjected to axial compression loads, the outer concrete tends to crush more readily than the concrete core, leading to an underutilization of the strength of the concrete core [23, 24]. To improve the mechanical performance of the outer concrete, Xu et al. [25] and Dai et al. [26] proposed the use of outsourcing angle steel to strengthen the concrete outside the steel tube. Yang et al. [27] suggested using the prestressed steel strips to strengthen the restraint of the concrete outside the steel tube. While these methods can enhance the mechanical properties of CFCST columns, they also present certain challenges, including complexity and high costs.

To overcome the problem of the CFCST columns, a new steel–concrete composite column, named a core-steel tube with T-shaped steel reinforced concrete (CSTRC) column, was proposed by Wang et al. [28] and Yaozong [29]. As shown in Figure 2, the new steel-composite column is composed of a steel tube with T-shaped steel embedded in a reinforced concrete column. Compared to CFCST columns, the T-shaped steel in the CSTRC column effectively restrains the deformation of the concrete outside the steel tube. This enhances the strength of the concrete, subsequently increasing the load-bearing capacity and ductility of the entire column. It can effectively address the issue of low utilization of strength in the concrete outside the steel tube in CFCST columns. Additionally, in comparison to existing reinforcement methods, the process of welding T-shaped steel outside the steel tube is

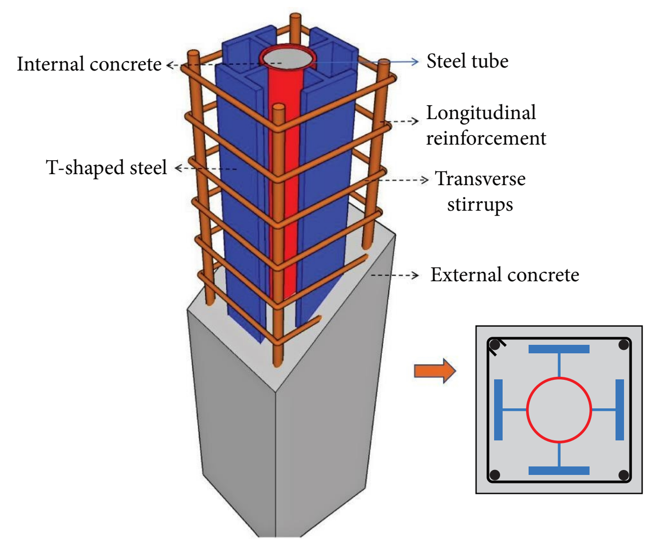

Figure 2: Core-steel tubes with T-shaped steel reinforced concrete (CSTRC) column.

straightforward, avoiding intricate procedures. The author has previously conducted research on the axial compression performance and seismic behavior of the CSTRC column. The results indicate that CSTRC columns exhibit high load-bearing capacity and deformation capability. Increasing the flange and web thickness of the T-shaped steel has minimal impact on enhancing the bearing capacity. In addition, with the increase in concrete strength, the load-bearing capacity of the column gradually increases, while ductility gradually decreases [28, 29].

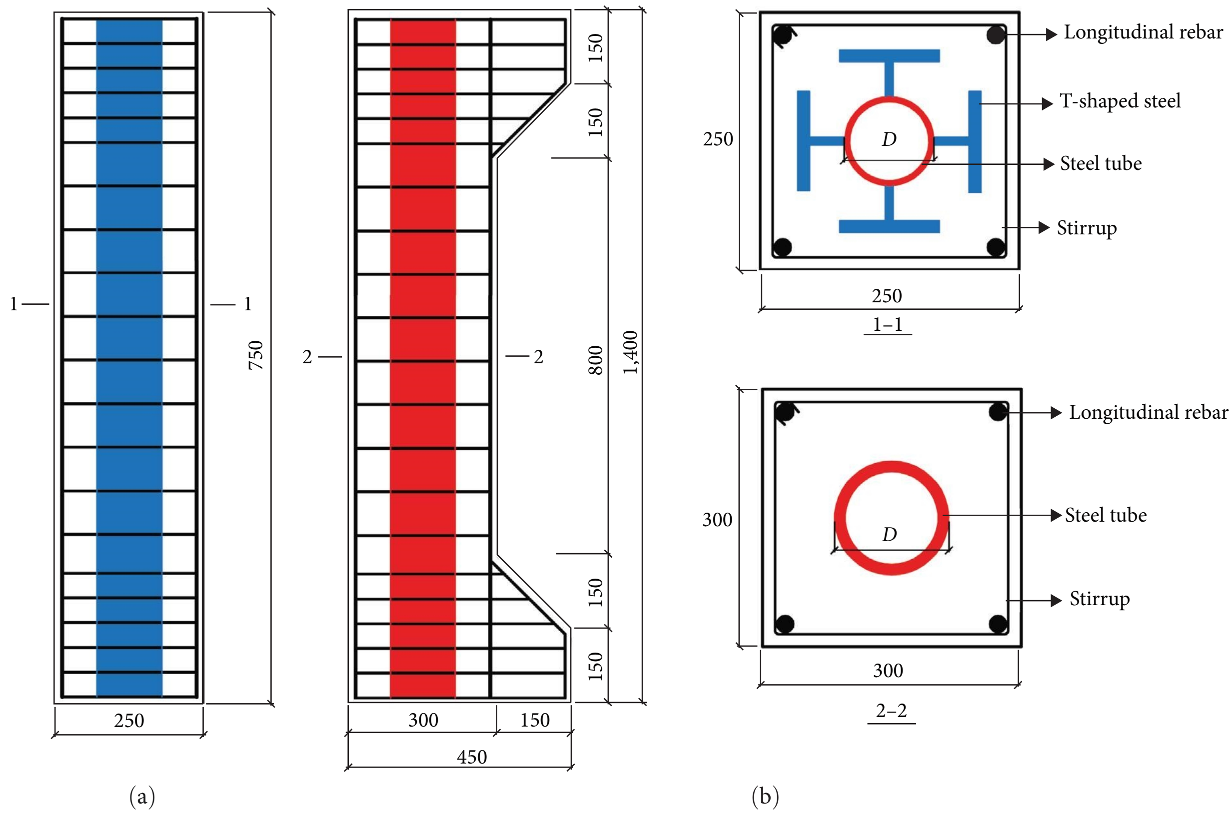

FIGURE 3: CFCST column specimens: (a) CSTRC column; (b) CFCST column.

Although conducted research has confirmed the favorable axial compression and seismic performance of CSTRC columns, the influence of various parameters on the eccentric compression ultimate load values and the corresponding design still need to be studied.

This paper investigates the eccentric compression behavior of CSTRC columns through numerical analysis. Initially, a finite element analysis (FEA) model is established, and the simulation results are compared with existing findings to validate the precision of the FEA model. Subsequently, the study delves into the performance of CSTRC columns under varying eccentricities, examining aspects such as load–deformation response, strain distribution, and stress distribution. Additionally, an exploration is conducted on the impact of parameters such as slenderness, concrete and steel strength, and steel ratio on the N_u–M_u interaction curves. Lastly, the paper proposes a set of formulas designed for calculating the eccentric bearing capacity of CSTRC columns.

2. The FEA Model

2.1. Basic Information. In order to verify the accuracy of the model, two distinct finite element models are established. One focuses on simulating the axial compression performance of CSTRC columns, while the other aspect involves the simulation of the eccentric compressive performance of CFCST columns. Except for the variation in loading conditions, the finite element modeling parameters remain identical for both models. The relevant experimental data is sourced from [28, 30], and the dimensions of the column specimens are shown in Figure 3. More details of the specimens can be found in literatures [28, 30]. Table 1 provides the primary test results.

2.2. Material Models. In this paper, the concrete damage plasticity model is used to model the nonlinear behavior of concrete. The uniaxial stress–strain curve proposed by Zhao et al. [31] is used to simulate the compressive performance of the T-shaped steel confined concrete. The stress–strain curve proposed by Han [32] is adopted to simulate the compressive performance of the steel tube confined concrete. The constitutive model provided in Chinese code (GB50010-2010) [33] is applied to the concrete cover; more details of the compressive stress–strain relationship can be found in literatures [31–33]. Moreover, the stress–strain curve suggested by the Chinese code (GB50010-2010) is used to express the tension behavior of the concrete, as shown by Equations (1) and (2). Because there is no T-shaped steel in the CFCST columns, the constitutive model in [31, 33] is used to simulate the compressive behavior of concrete inside and outside steel tube, respectively. The stress-inelastic strain values of the concrete in compression are listed in Table 2.

$$\sigma = (1 - d_t)E_c\varepsilon, \tag{1}$$

$$d_t = \begin{cases} 1 - \rho_t(1.2 - 0.2x^5)x \le 1 \\ 1 - \dfrac{\rho_t}{\alpha_t(x-1)^{1.7} + x}x \ge 1 \end{cases}, \tag{2}$$

Table 1: Comparison of ultimate strength between FEA results (N_{num}) and experimental results (N_{exp}).

References	Specimens	B (mm)	$D \times t$ (mm)	f_{ys} (MPa)	ρ_s (%)	e (mm)	N_{exp} (kN)	N_{num} (kN)	N_{num}/N_{exp}
[28]	CRSTRC1	250	90 × 5	363	1.3	—	4,872	4,883	1.00
	CRSTRC2	250	90 × 5	363	1.3	—	4,967	5,094	1.03
	CRSTRC3	250	90 × 5	363	1.3	—	4,926	4,992	1.01
	CRSTRC4	250	90 × 5	363	1.3	—	5,090	5,076	1.00
	CRSTRC5	250	90 × 5	363	1.3	—	5,096	4,949	0.97
	CRSTRC6	250	90 × 5	363	1.3	—	4,960	5,063	1.02
	CRSTRC7	250	90 × 5	363	1.3	—	4,760	4,885	1.03
	CRSTRC8	250	90 × 5	363	1.3	—	4,921	5,069	1.03
	CRSTRC9	250	90 × 5	363	1.3	—	4,967	5,112	1.03
[30]	CFCST-1	300	133 × 4.5	339	0.89	50	2,210	2,203	1.00
	CFCST-2	300	133 × 4.5	339	0.89	100	1,427	1,348	0.94
	CFCST-3	300	133 × 4.5	339	0.89	130	1,111	1,069	0.96
	CFCST-4	300	133 × 4.5	339	0.89	150	922	865	0.94
	CFCST-5	300	133 × 4.5	339	0.89	190	602	616	1.02
	CFCST-6	300	133 × 4.5	339	0.89	220	501	521	1.04
	CFCST-7	300	89 × 7	339	0.89	190	531	576	1.08
	CFCST-8	300	102 × 6	339	0.89	190	573	608	1.06
	CFCST-9	300	168 × 3.5	339	1.00	190	611	657	1.08
	CFCST-10	300	133 × 4.5	339	1.58	190	660	705	1.07
	CFCST-11	300	133 × 4.5	339	2.11	190	671	754	1.12
	CFCST-12	300	133 × 4.5	339	2.64	190	791	816	1.03
			Average ratio of numerical to measured value						1.02
			Standard deviation						0.05

Note. B represents the width of the cross-section of specimens; D and t in order represent the steel tube outside diameter and thickness; f_{ys} denotes the steel tube strength; ρ_s is the reinforcement ratio, and e is the eccentric distance.

Table 2: Properties of the concrete in compression

Reference [28]			Reference [30]		
Compression stress	Inelastic strain	Damage parameter	Compression stress	Inelastic strain	Damage parameter
35.35	0.0000548	0.02500	32.37	0.0000781	0.03703
39.69	0.0001103	0.04353	36.01	0.0001451	0.05968
42.95	0.0001979	0.06924	38.65	0.0002429	0.08875
44.95	0.0003234	0.10234	40.20	0.0003740	0.12373
45.60	0.0004888	0.14222	40.70	0.0005377	0.16357
42.47	0.0009522	0.24430	38.23	0.0009718	0.26000
36.41	0.0015033	0.35225	33.31	0.0014810	0.36044
30.46	0.0020509	0.44580	28.33	0.0019922	0.44828
25.54	0.0025678	0.52156	24.09	0.0024809	0.52040
21.66	0.0030534	0.58195	20.66	0.0029443	0.57861
18.64	0.0035136	0.63027	17.93	0.0033863	0.62570
16.26	0.0039547	0.66939	15.75	0.0038114	0.66415

where $x = \varepsilon/\varepsilon_t$; $\rho_t = f_t/E_c\varepsilon_t$, and f_t denotes the concrete tensile strength; E_c is the elastic modulus of concrete.

The stress–strain relationship of the steel adopts the ideal elastic–plastic model, as shown in Figure 4, which is stated by the following:

$$\sigma_s = \begin{cases} E_s\varepsilon_s & \varepsilon_s \le \varepsilon_y \\ f_y & \varepsilon_s \ge \varepsilon_y \end{cases}, \tag{3}$$

where E_s is the elastic modulus of steel; f_y denotes the steel yield strength; ε_y represents the steel yield strain.

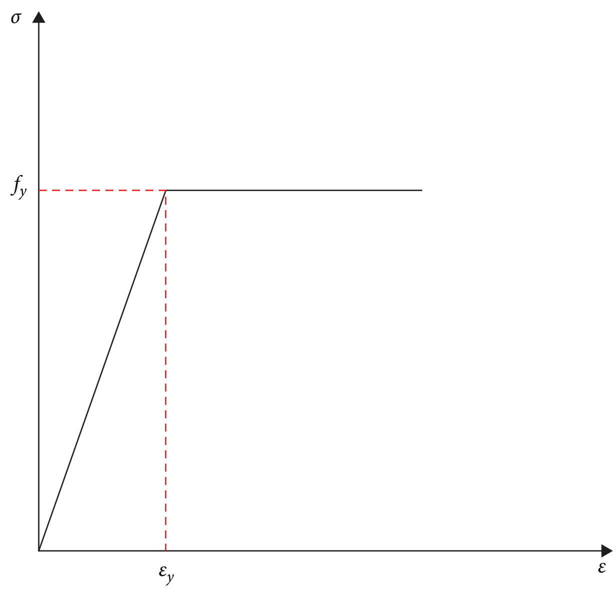

Figure 4: Stress–strain relationships of steel.

2.3. Element Type and Mesh Size. The concrete, steel tube, and end plates of the specimens are modeled by C3D8R elements. The longitudinal and transverse reinforcement steel bars are modeled by T3D2 elements. A convergence analysis is conducted to determine suitable mesh sizes, thereby improving both the convergence and computational efficiency of the FEA model. According to the results of the convergence analysis, the optimal size for the concrete and steel tube is established at 30 mm, while the size of the steel bars is set at 35 mm.

2.4. Contact Relation and Boundary Conditions. For CFCST columns with a smooth steel tube surface, the interface between the steel tube and concrete is prone to slipping. Consequently, it becomes imperative to employ an appropriate approach for simulating the failure of this interface in finite element modeling. Currently, the coulomb friction stands out as a widely accepted method to emulate the contact behavior between the steel pipe and concrete. The reliability of this method has been substantiated by pertinent research studies [34, 35]. As a result, an interface model combining the "hard" contact model in the normal direction and the coulomb friction model in the tangential direction is used to replicate the interaction behavior between the concrete and the steel tube in the paper. The friction coefficient used at the interface of the concrete and the steel tube is 0.4. The interaction between the end plates and the steel tube is simulated by "tie" contact. The interaction between the end plates and the concrete is simulated by surface-to-surface contact. To facilitate the convergence of FEA models, the slip between reinforcement and concrete is not considered. Thus, the interaction between the reinforcement and the concrete is simulated by "embedded."

As depicted in Figure 5, the eccentric compression load is administered to the loading line on the top-end plate of the specimens. The upper part of the specimens is allowed translational movement along the y-axis and rotational movement around the z-axis, while other degrees of freedom are constrained. On the bottom surface of the end plate, translation in the x, y, and z directions is restricted, and rotation around the x and y axes is not permitted. For CSTRC columns subjected to axial loads, the translation and rotation of the column base in the x, y, and z directions are entirely constrained.

2.5. Verification

2.5.1. Ultimate Strength. Figure 6 presents the comparison of the ultimate strength obtained from the FEA and the test, and Table 1 lists the corresponding values. The average of the $N_{\mathrm{num}}/N_{\mathrm{exp}}$ is 1.02, the standard deviation is 0.05, and the maximum error is 12%. As a result, the simulated results are agree well with the experimental results.

2.5.2. Load–Displacement Response. Figure 7 presents a comparison of the load–displacement curves for specimens as documented in [28]. The results illustrate that the finite element model can well reflect the axial compression behavior of CSTRC columns. The simulated load–displacement curves closely align with the experimental data.

2.5.3. Load–Strain Response. Figure 8 shows the comparison of the load–longitudinal steel tube strain curves of specimens in reference [30]. It can be seen that, for specimen CFCST-3 with an eccentric distance (e) of 130 mm, the load–strain curves of the tensile and compression zones of the steel tube, as obtained from the finite element model, closely align with the experimental results. In the case of specimen CFCST-9 with an eccentric distance of $e = 190$ mm, although the simulated strain growth rate is slightly lower than the experimental results, the overall trend of the curves remains consistent. Based on the above comparisons, it is considered that the FEA model has high accuracy, and it can be used to further investigate the eccentric mechanical properties of CSTRC columns.

3. Analytical Behavior

A finite element model is established for the comprehensive exploration of the eccentric compressive properties of CSTRC columns, with the detailed specimen dimensions depicted in Figure 9. The specimen features a cross-section size of 400 mm × 400 mm and a length of 1,600 mm, with the steel skeleton measuring 340 mm × 340 mm in cross-section. The steel tube's outside diameter (D) is 250 mm, and its thickness (t) is 2 mm. The concrete strength (f_{cu}) inside and outside the steel tube is 40 MPa. The steel tube and T-shaped steel strength (f_{ys}) is 345 MPa. The steel bar's strength (f_y) is 335 MPa.

3.1. Load–Deformation Response. In Figure 10, the axial load (N) and lateral deflection (μ_{m}) curves for specimens with varying eccentricity ratios are presented. Notably, at lower loads, the load–deformation curves exhibit a linear relationship. As the eccentricity increases, there is a noticeable reduction in both the initial stiffness and peak load of the specimen. Specifically, as the eccentricity ratios increase from 0.2 to 0.5 and from 0.5 to 0.8, the ultimate load experiences a reduction of 49.4% and 39%, respectively. This observation indicates

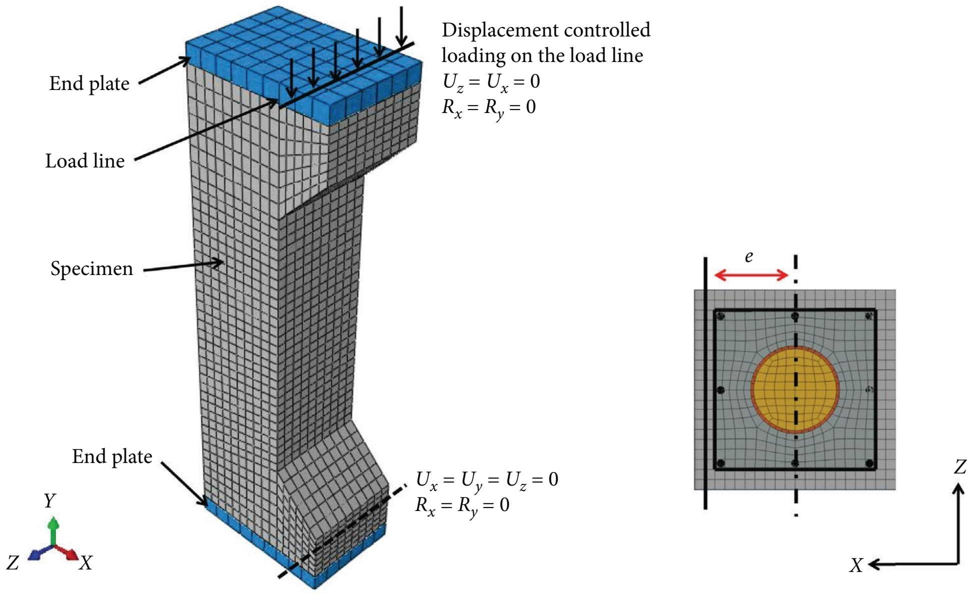

FIGURE 5: Finite element model of CFCST columns: (a) general view; (b) cross-section.

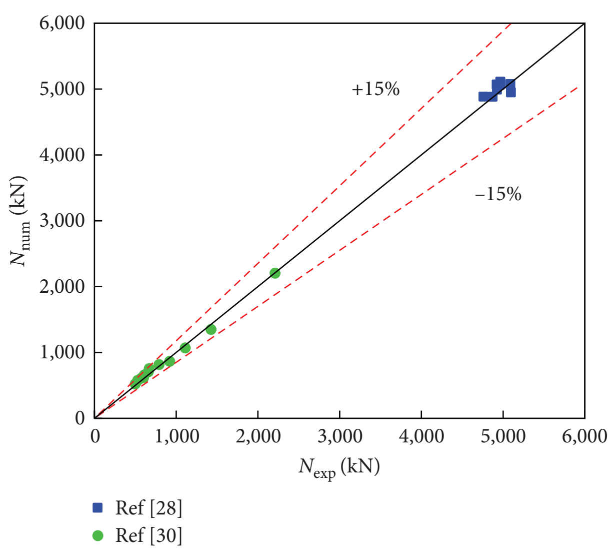

FIGURE 6: Comparison between FEA (N_{num}) and experimental results (N_{exp}).

that the eccentricity has a great effect on the ultimate strength of the CSTRC columns.

3.2. Load–Strain Response. In Figure 11, the strain development of concrete and steel in columns with various eccentricity ratios is illustrated. The strain distributions along the height of the middle cross-section of the specimens exhibit linearity, confirming adherence to the plane section assumption. Specifically, for the specimen with an eccentricity ratio of $e/B = 0.2$, upon reaching the peak load (N_u), the concrete in the compression area is crashed, and the ultimate compression strain reaches 3385 $\mu\varepsilon$. Simultaneously, the compression strain of the steel is 3,114 $\mu\varepsilon$, and the tensile strain is 477 $\mu\varepsilon$, with no yielding observed in the steel at the tensile area. This suggests that, for an eccentricity ratio of $e/B = 0.2$, the strain development in the cross-section of CSTRC columns accords with the small eccentric compression failure. In Figure 11(b), when the specimen with an eccentricity ratio of $e/B = 0.5$ reaches the ultimate load, the tensile strain of the steel measures 1,963 $\mu\varepsilon$, and the compression strain of the concrete amounts to 3,538 $\mu\varepsilon$. This observation suggests that both the concrete and the steel have undergone yielding at this stage.

In the case of the specimen with an eccentricity ratio of $e/B = 0.8$, at 0.95 N_u, the steel tensile strain is 1,840 $\mu\varepsilon$, while the compression strain of the concrete is 2,270 $\mu\varepsilon$, with the concrete exhibiting no yielding. Upon reaching the peak load N_u, the concrete undergoes yielding with a compression strain of 3,421 $\mu\varepsilon$. This observation indicates that, for an eccentricity ratio of $e/B = 0.8$, the strain development in the cross-section of CSTRC columns accords with the large eccentric compression failure.

3.3. Load–Stress Response

3.3.1. Steel Stress. Figure 12 demonstrates the stress development of the steel of the columns with various eccentricity ratios. For the CSTRC column with an eccentricity of $e/B = 0.2$, when the load reaches N_u, the middle-height section of the steel is predominantly compressed, with only a small area experiencing tension. For columns with an eccentricity of $e/B = 0.5$, the stress development in the tension area is slower than that on the compression side. Notably, in the case of the CSTRC column with an eccentricity of $e/B = 0.8$, the stress in the tension zone grows more rapidly than that in the compression zone. This indicates that, with the increase of eccentricity, the failure mode of CSTRC columns shifts from compression control to tension control.

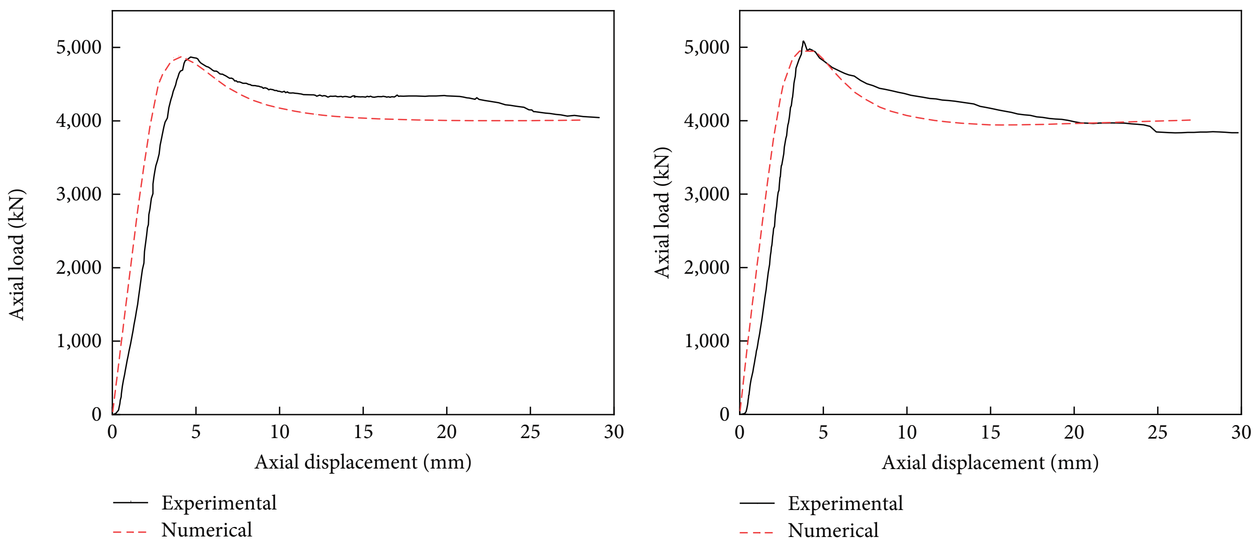

(a) (b)

FIGURE 7: Comparison between FEA and experimental load–displacement curves: (a) CRSTRC1; (b) CRSTRC5.

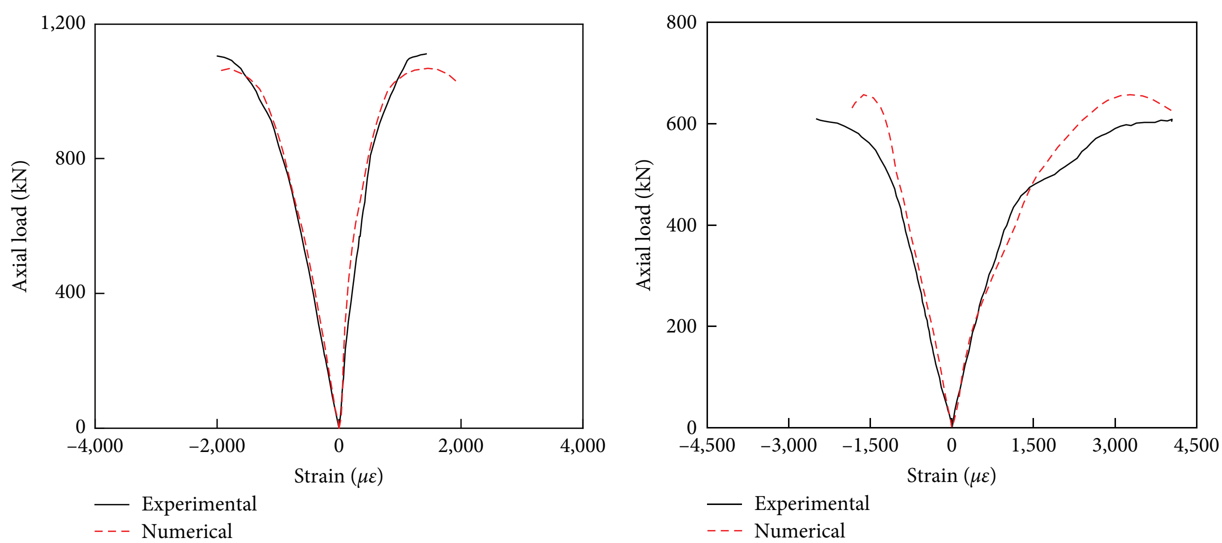

(a) (b)

FIGURE 8: Comparison between FEA and experimental load–strain curves: (a) CFCST-3; (b) CFCST-9.

3.3.2. Concrete Stress. Figure 13 presents the longitudinal stress (s33) distribution of the concrete across the middle height section at the ultimate state. Notably, the neutral axis shifts from the edge to the middle with an increase in the eccentricity ratio. When the eccentricity ratio is $e/B = 0.2$, the value of s33 for the confined concrete is 1.11 times that of the unconfined concrete. However, the value of s33 of the confined concrete is 0.9 times that of the unconfined concrete when the eccentricity ratio $e/B = 0.8$. With the increase in eccentricity, s33 on the compression side gradually diminishes. This phenomenon suggests that as the eccentricity ratio increases, the constraint provided by the steel skeleton to the concrete in the compression zone tends to decrease, leading to a corresponding weakening bearing capacity of concrete.

3.4. Parametric Analysis. To gain a deeper insight into the eccentric mechanical properties of CSTRC columns, an initial examination is conducted on the N_u–M_u interaction curves for columns with varying slenderness ratios (λ). Subsequently, based on the findings, the impact of concrete and steel strength, as well as steel ratio, on the N_u–M_u interaction curves of CSTRC columns with two distinct slenderness ratios are further discussed. The concrete strength values (f_{cu}) used are 30, 40, and 50 MPa, respectively. The steel strength (f_{ys}) used is 235, 345, and 400 MPa, respectively.

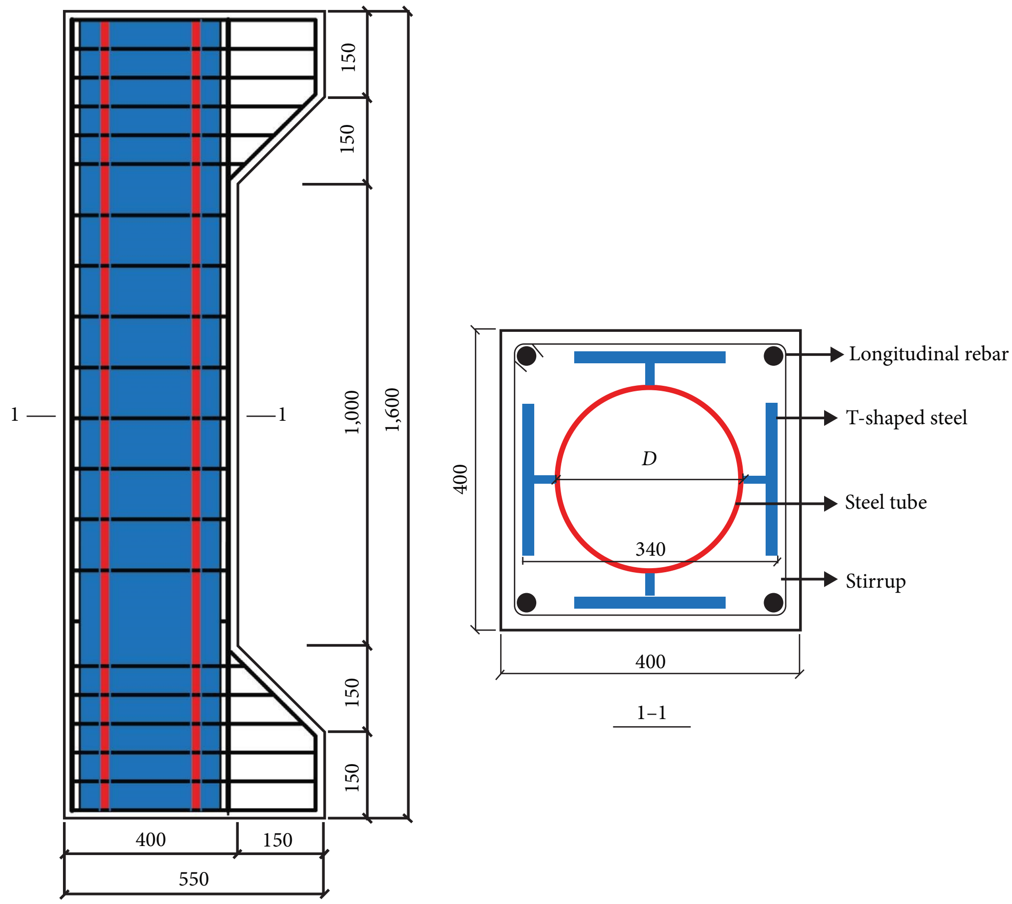

Figure 9: CSTRC column specimens.

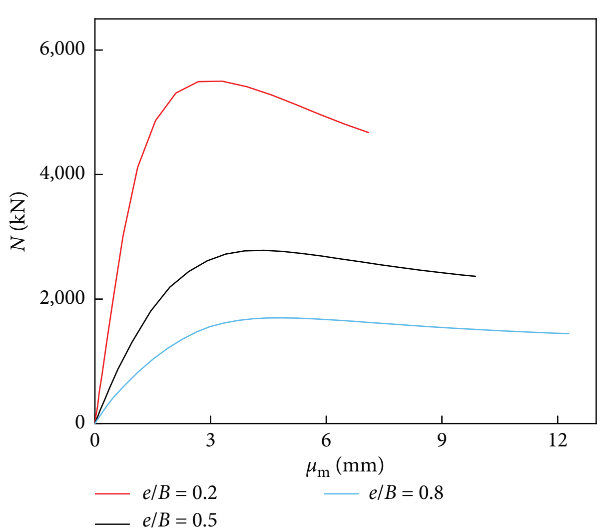

Figure 10: Axial load versus mid-height lateral deflection.

Additionally, the steel ratio (α_s) is explored at values of 4%, 6%, and 8%, respectively.

3.4.1. Effect of Slenderness Ratio. The slenderness ratio significantly impacts the mechanical performance of the columns. If the slenderness of columns falls below a certain value, denoted as λ_{lim}, the second-order effect can be disregarded, and such columns are typically classified as short columns. However, for long columns with a slenderness ratio exceeding λ_{lim}, significant lateral deformation occurs under eccentric loading. In such cases, the influence of the second-order effect should be taken into consideration. Eight CSTRC column specimens with different slenderness ratios are simulated to investigate the influence of slenderness ratio on N_u–M_u interaction curves, which correspond to a range of slenderness ratios of 15, 22, 29, 40, 50, 60, 70, and 85, respectively. The study results are presented in Figure 14.

Figure 14(a) presents the N_u–M interaction curves of specimens with $\lambda = 22$ and $\lambda = 29$. M_1 represents the first moment. M_u denotes the total bending moment, including the second-order moment. The parameter c is utilized to characterize the increased amplitude of the total bending moment, calculated as $c = (M_u - M_1)/M_1$. When the slenderness ratio is $\lambda = 22$, the value of c remains within 10%. However, for $\lambda = 29$, the value of c exceeds 10%. Eurocode 2 [36] mentioned that when the value of c is less than 10%, the second-order effect on columns can be ignored. Hence, the slenderness ratio limit λ_{lim} is 22 for CSTRC columns. When λ_{lim} exceeds 22, the influence of the second-order effect on the total bending moment should be considered.

Figure 14(b) demonstrates the N_u–M_1 interaction curves of specimens with various slenderness ratios. It is observed

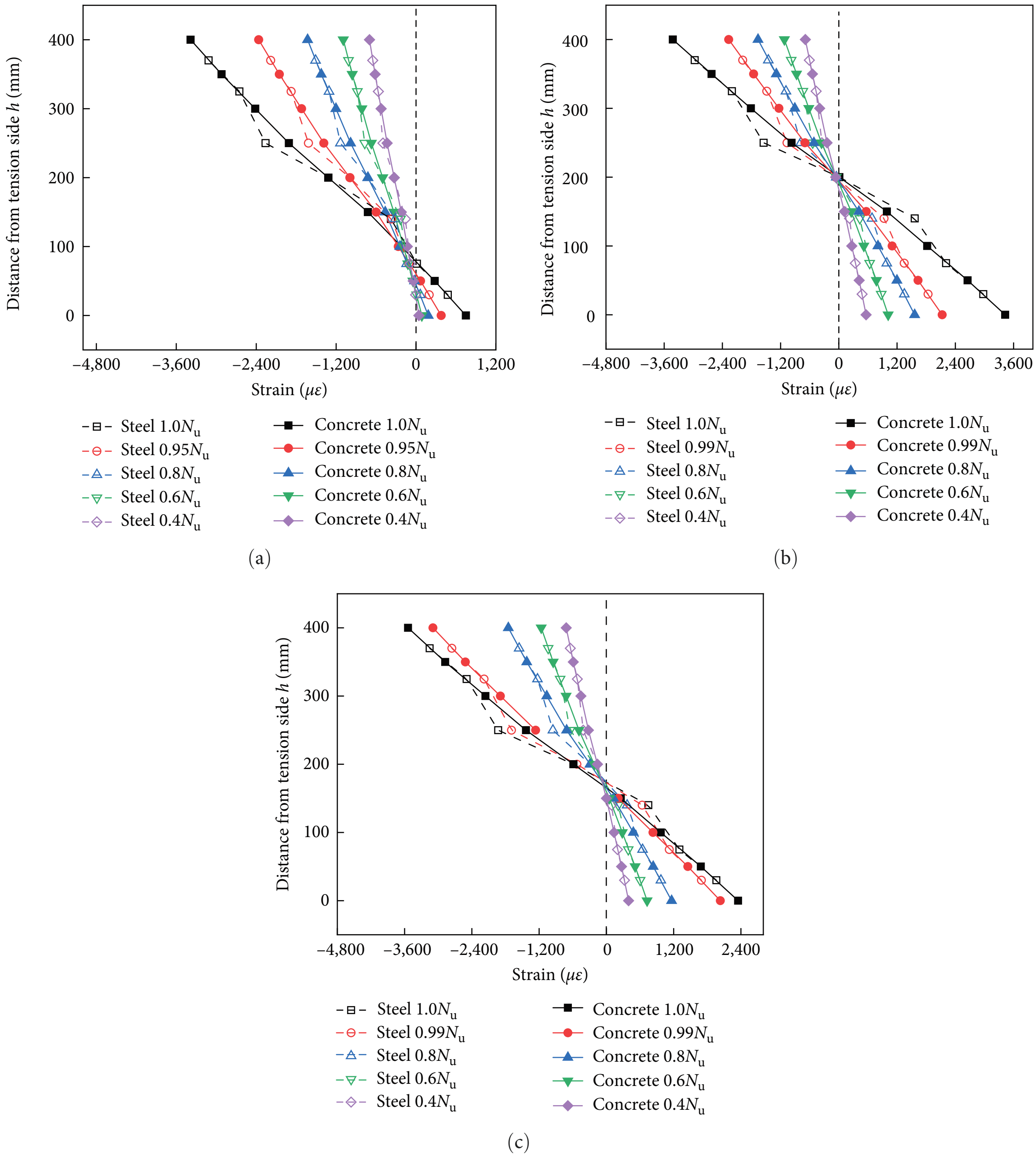

FIGURE 11: Strain distribution of steel and concrete along the height of the mid-span point section: (a) $e/B = 0.2$; (b) $e/B = 0.5$; (c) $e/B = 0.8$.

that, with the increase in eccentricity, the value of M_1 initially rises and then declines for the specimens with $\lambda = 15$–60. Nevertheless, for the specimens with $\lambda = 60$–85, there is a continuous increase in the value of M_1. This phenomenon can be attributed to distinct failure modes in the specimens. For these specimens with $\lambda = 60$–85, instability failure is the main failure mode, and the material strength of specimens cannot be fully utilized. Conversely, for the specimens with $\lambda = 15$–60, the failure of columns is mainly caused by the failure of material strength.

3.4.2. Effect of Other Parameters. This section explores the influence of concrete and steel strength, as well as steel ratio, on the N_u–M_u interaction curves of CSTRC columns with two distinct slenderness ratios. Short columns have a length (l_0) of 1,600 mm, with a slenderness ratio of $\lambda = 14$, while long columns have a length (l_0) of 3,200 mm, with a slenderness ratio of $\lambda = 28$. The results of the parametric studies are presented in Figure 15.

As expected, the N_u–M_u interaction curves for specimens with both slenderness ratios expand outward with

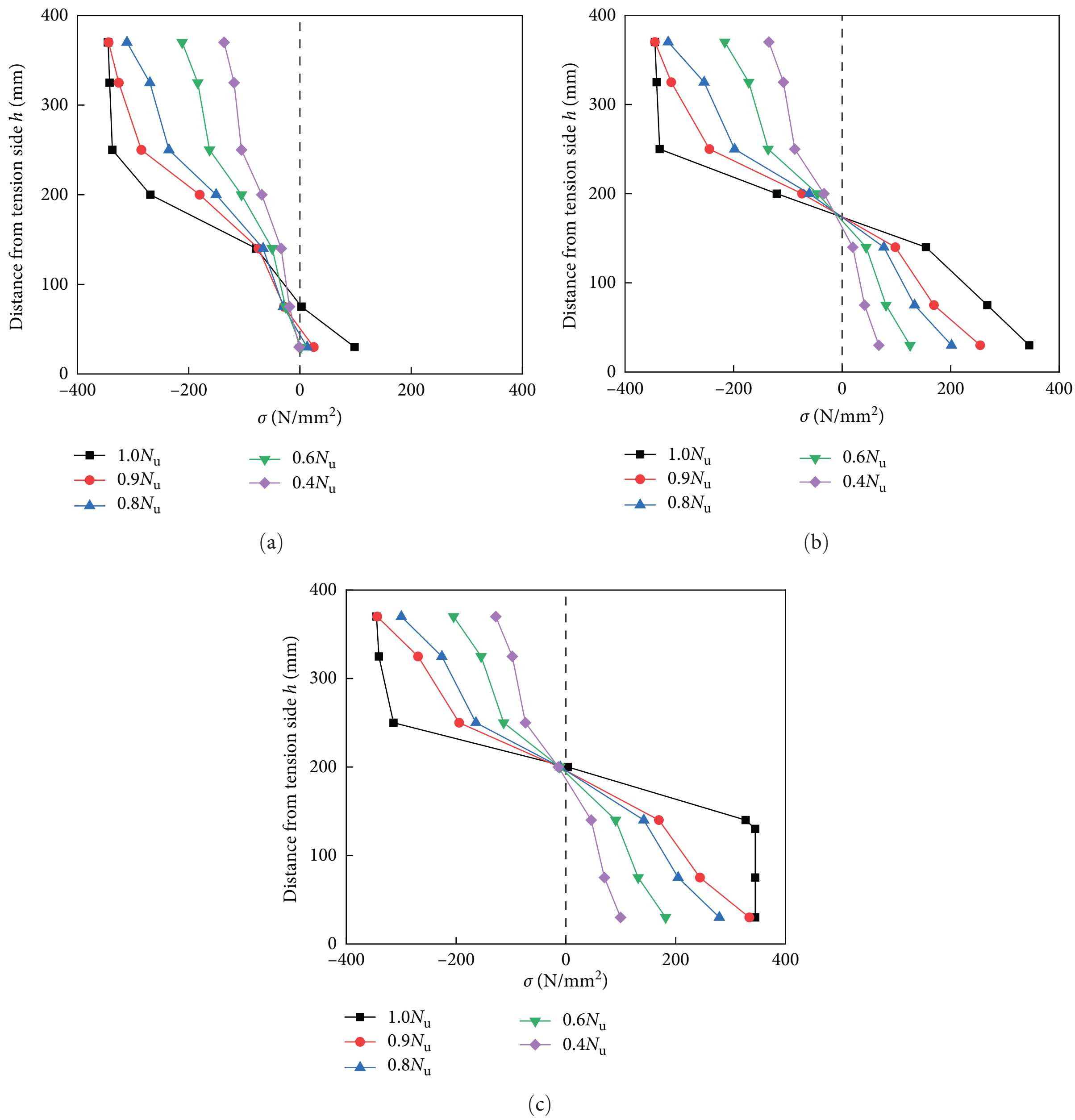

Figure 12: The stress distribution of steel along the height of the mid-span point section: (a) $e/B = 0.2$; (b) $e/B = 0.5$; (c) $e/B = 0.8$.

the increase of f_{cu}, f_{ys}, or α_s, indicating a rise in the ultimate load values of CSTRC columns. Moreover, in comparison to the specimens with different lengths, short CSTRC columns exhibit higher strength than long CSTRC columns. For specimens with large eccentricity, the increase in capacity in the region below the balanced failure point on the N_u–M_u interaction curves is less pronounced as f_{cu} increases. This is attributed to the relatively small concrete tensile strength, limiting the increase in moment capacity. In addition, as the f_{ys} or α_s increase, both the load and moment capacities increase. The main reason is that the tensile and compressive strength of steel is basically the same, which can contribute both to the axial load and bending moment of the specimen.

4. Analysis on Bearing Capacities

4.1. Calculation Methods. The complex steel skeleton section of CSTRC columns introduces complexity in calculations. Consequently, according to the Chinese code (JGJ138-2016) [37], the cross-section of the steel skeleton is simplified as an I-shaped section, as shown in Figure 16. The equivalent steel web thickness can be evaluated as follows:

$$t'_w = \frac{t_w(h_w - D) + 0.5\sum A_{af} + 0.5A_g}{h_w}, \tag{4}$$

where t'_w and h_w in order denote the steel web thickness and length; $\sum A_{af}$ represents the sectional area of the steel flanges

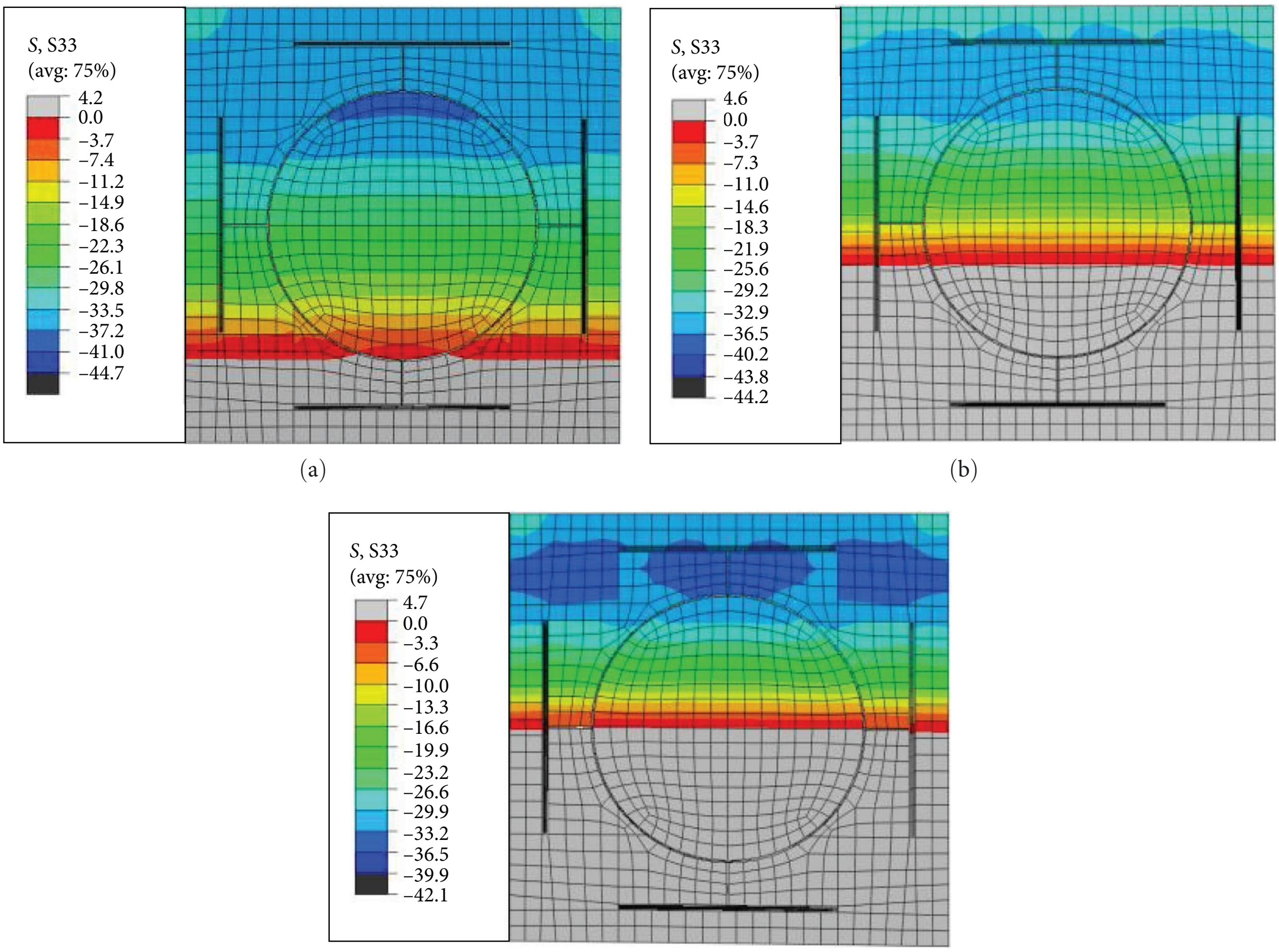

(c)

Figure 13: The longitudinal stress (S33) distribution of concrete at the ultimate state: (a) $e/B = 0.2$; (b) $e/B = 0.5$; (c) $e/B = 0.8$.

perpendicular to the load direction; A_g represents the steel tube cross-sectional area; t_w denotes the thickness of the steel web of the T-shaped steel.

Under eccentric loads, the steel tube and T-shaped steel restrain the deformation of the concrete, offering confining pressure. It is assumed that the confinement effectiveness coefficient is denoted as k. The value of k can be evaluated from literature [29]. Additionally, some assumptions are made that: (1) the tension strength of concrete is neglected; (2) the strain development of the steel and the concrete accord with the plane section assumption.

4.2. Calculation of Bearing Capacity of Large Eccentricity Columns. Due to the proximity of the steel flanges of the CSTRC column to the edge of the concrete cover, the steel flange strength in the compression zone can reach its yielding strength. Therefore, the calculation of the ultimate strength of the CSTRC column considers only one case: $h_1 < x \le x_b$, where x is the length of the compression area; x_b is the balanced length of the compression area. For the specimens with large eccentricity, this implies that both the steel flange sections in the compression and tension areas reach yield. Figure 17 shows the stress–strain diagram, and the bearing capacity N_u can be calculated based on the force equilibrium condition as follows:

$$N_u = \alpha_1 f_c b \beta_1 x + (k-1)\alpha_1 f_c b_1(\beta_1 x - h_1) + (2x - \delta_2 h - h_1) t'_w f_{yw}, \tag{5}$$

$$\begin{aligned} N_u\left(e - \frac{h}{2} + x\right) = {} & \alpha_1 f_c b \beta_1 x\left(x - \frac{\beta_1 x}{2}\right) + (k-1)\alpha_1 f_c b_1(\beta_1 x - h_1)\left(x - \frac{\beta_1 x - h_1}{2}\right) \\ & + t'_w f_{yw}\left(\frac{2}{3}d^2 + (x - h_1 - d)\frac{(x - h_1 + d)}{2} + (h_1 + h_2 - x - d)\frac{(h_1 + h_2 - x + d)}{2}\right) \\ & + f_y A'_s(h - 2a'_s) + f_{af} A'_{af}(h - 2a'_a), \end{aligned} \tag{6}$$

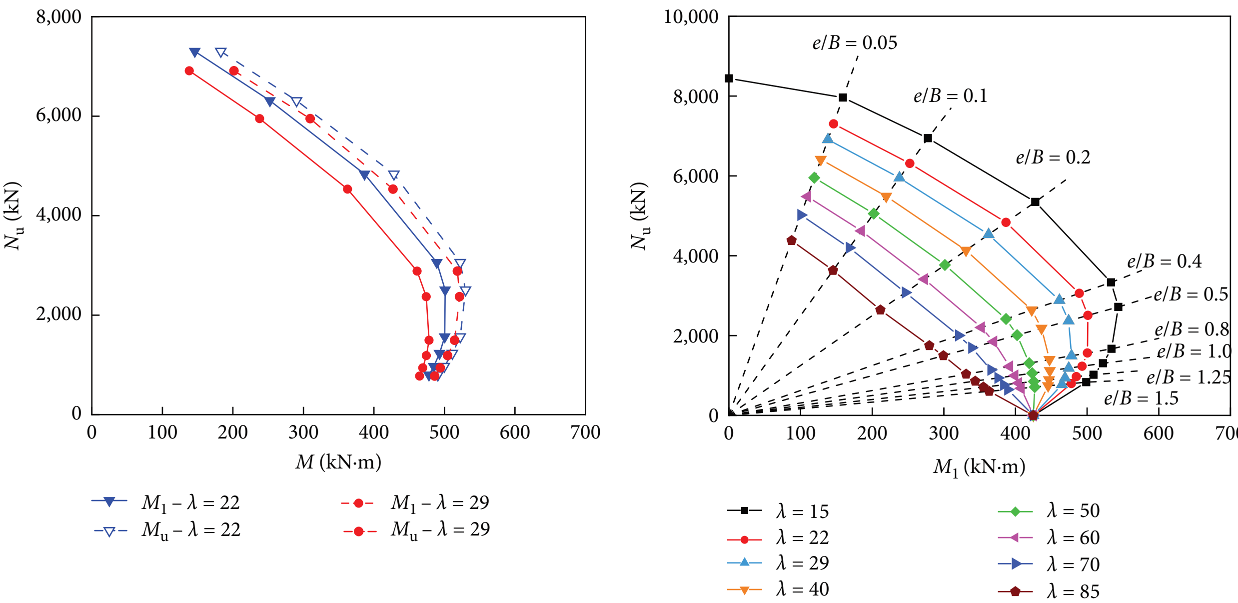

(a) (b)

FIGURE 14: Influence of slenderness ratio (λ) on N_u–M_u interaction curves: (a) N_u-M; (b) N_u-M_1.

$$d = \frac{f_{yw}}{\varepsilon_{cu} E_s} x, \tag{7}$$

$$x_b = \frac{1}{1 + \frac{f_{af}}{\varepsilon_{cu} E_s}} (h - a_a). \tag{8}$$

4.3. Calculation of Bearing Capacity of Small Eccentricity Columns. For the CSTRC column with small eccentricity, the steel flange close to the loading point can reach yielding strength, but the flange far from the loading point may not reach its yielding strength. Therefore, there are two cases of internal force distribution on the cross-section of the CSTRC, as shown in Figures 18 (a) and 18(b). The two cases are shown as follows:

Case 1: when $x_b < x \leq h - a_a$, the steel section above the neutral axis yields under compression, but the steel section below the neutral axis does not yield. The stress–strain relation, as shown in Figure 18(a), and the N_u can be denoted as follows:

$$\begin{aligned} N_u = {} & \alpha_1 f_c b \beta_1 x + (k-1)\alpha_1 f_c b_1 (\beta_1 x - h_1) + (x - h_1 - d) t'_w f_{yw} \\ & + \frac{1}{2}\left(\sigma_{af} + f_{yw}\right) t'_w (d + x - \delta_2 h) + f_y A'_s + f_a A'_{af} \\ & - \sigma_s A_s - \sigma_{af} A_{af}, \end{aligned} \tag{9}$$

$$\begin{aligned} N_u\left(e - \frac{h}{2} + x\right) = {} & \alpha_1 f_c b \beta_1 x \left(x - \frac{\beta_1 x}{2}\right) + (k-1)\alpha_1 f_c b_1 (\beta_1 x - \delta_1 h)\left(x - \frac{\beta_1 x - h_1}{2}\right) \\ & + t'_w f_{yw} (x - h_1 - d)\frac{(x - h_1 + d)}{2} + \frac{1}{3} t'_w f_{yw} d^2 + \frac{1}{3} t'_w \sigma_{af} (h_1 + h_2 - x)^2 + f_y A'_s (x - a'_s) \\ & + f_{af} A'_{af} (x - a'_a) + \sigma_s A_s (h - x - a_s) + \sigma_{af} A_{af} (h - x - a_a) \end{aligned}, \tag{10}$$

$$\sigma_{af} = \frac{(h - a_a - x)}{x} \varepsilon_{cu} E_s \leq f_{af}, \tag{11}$$

$$\sigma_s = \frac{(h - a_s - x)}{x} \varepsilon_{cu} E_s \leq f_y. \tag{12}$$

Case 2: when $x_b < x \leq h - a_a$, the whole section is in compression, but the steel section far from the loading point is not yield under compression, as shown in Figure 18(b). The value of N_u can be evaluated by Equations (13)–(16).

$$\begin{aligned} N_u = {} & \alpha_1 f_c b \beta_1 x + (k-1)\alpha_1 f_c b_1 (\beta_1 x - h_1) + (x - h_1 - d) t'_w f_{yw} \\ & + \frac{1}{2}\left(\sigma_{yw} + f_{yw}\right) t'_w (d - x + \delta_2 h) + f_y A'_s + f_{af} A'_{af} \\ & + \sigma_s A_s + \sigma_{af} A_{af}, \end{aligned} \tag{13}$$

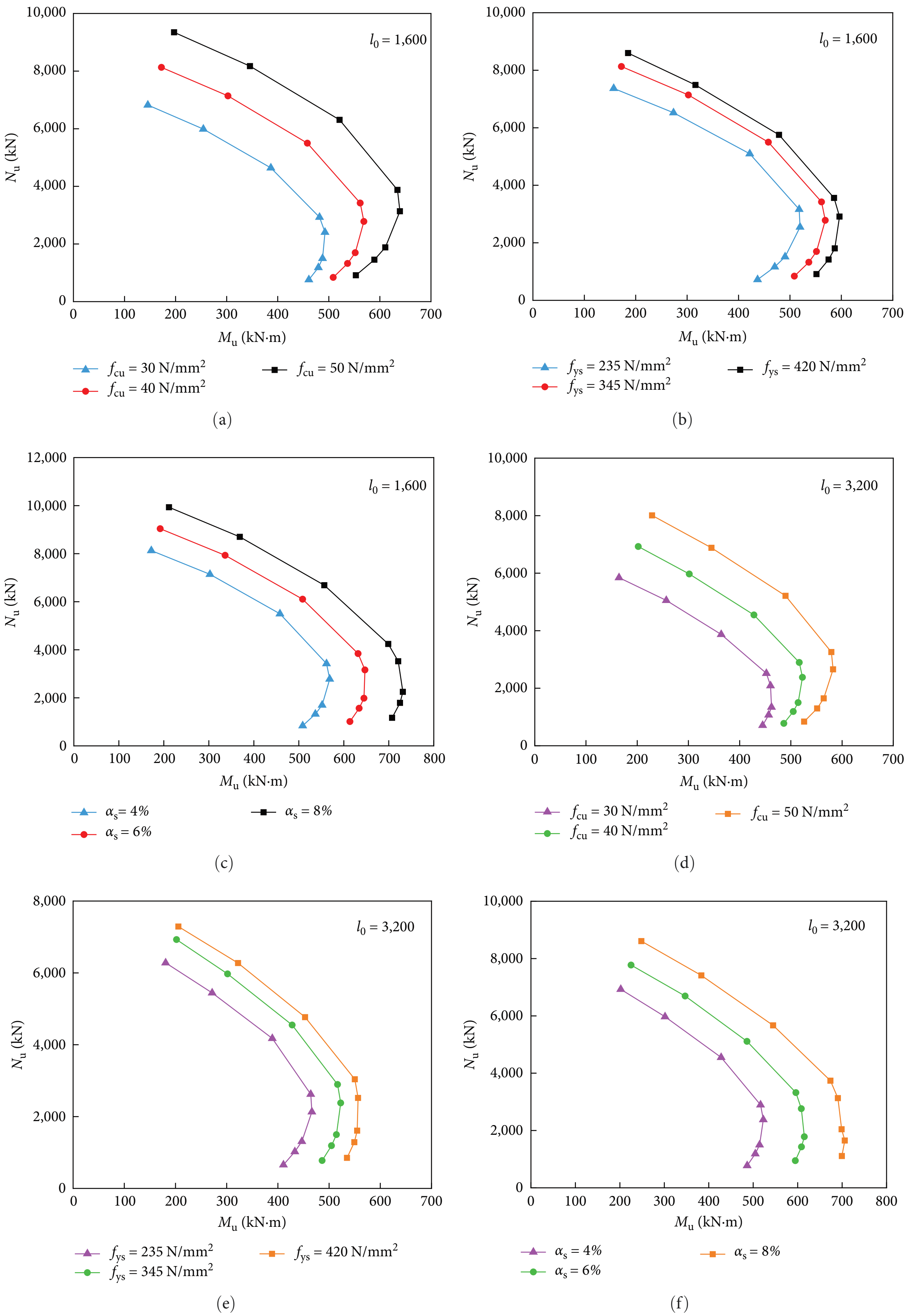

Figure 15: Influence of various parameters on N_u–M_u interaction curves: (a) f_{cu}; (b) f_{ys}; (c) α_s; (d) f_{cu}; (e) f_{ys}; (f) α_s.

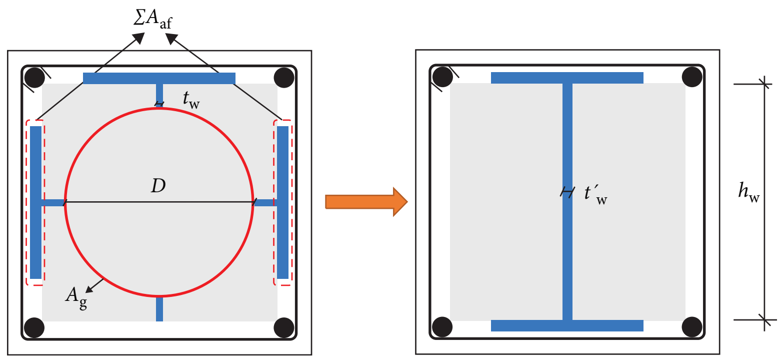

FIGURE 16: Simplified the cross-section of the steel skeleton of the CSTRC column.

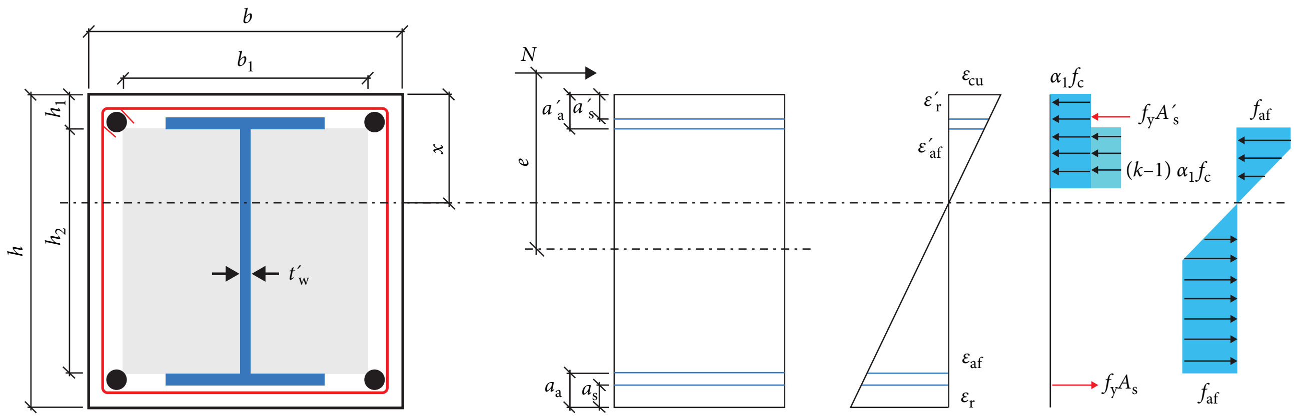

FIGURE 17: Stress–strain diagram of large eccentricity failure specimen.

$$
\begin{aligned}
N_u\left(e-\frac{h}{2}+x\right) &= \alpha_1 f_c b\beta_1 x\left(x-\frac{\beta_1 x}{2}\right)+(k-1)\alpha_1 f_c b_1(\beta_1 x-h_1)\left(x-\frac{\beta_1 x-h_1}{2}\right)\\
&\quad + t'_w f_{yw}(x-d-h_1)\left(\frac{x-h_1+d}{2}\right)+\frac{1}{2}(\sigma_{af}+f_{yw})t'_w(h_1+h_2-x+d)\left(\frac{x+d-h_1-h_2}{2}\right)\\
&\quad + f_y A'_s(x-a'_s)+f_{af}A'_{af}(x-a'_a)+\sigma_s A_s(x-h+a_s)+\sigma_{af}A_{af}(x-h+a_a),
\end{aligned}
\tag{14}
$$

$$\sigma_{af}=\frac{(x-h+a_a)}{x}\varepsilon_{cu}E_s\le f_{af}, \tag{15}$$

$$\sigma_s=\frac{(x-h+a_s)}{x}\varepsilon_{cu}E_s\le f_y, \tag{16}$$

where b and h in order represent the width and the height of the cross-section of specimens; b_1 denotes the width of the equivalent rectangular; h_1 denotes the distance from the upper steel flange to the edge of the section of the specimen; h_2 is the distance between the upper and lower flange of the shape steel; x denotes the depth of the concrete in compression area; α_1 and β_1 represent the equivalent rectangular coefficient, and $\alpha_1=1, \beta_1=0.8$. f_c represents the concrete compressive strength; ε_{cu} represents the concrete ultimate compressive strain, and $\varepsilon_{cu}=0.0033$; f_y denotes the longitudinal reinforcement yielding strength; A'_s and A_s represent the longitudinal reinforcement cross-section areas in compression tension area and in tension area, respectively; f_{af} denotes the flange yielding strength; σ'_{af} and σ_{af} represent the steel stress in compression area and in tension area, respectively; A'_{af} and A_{af} represent the steel flange cross-section areas in compression area and in tension area, respectively; f_{yw} denotes the steel web yielding strength; a_s denotes the distance from the tensile longitudinal bars centroid to the edge of columns; a'_s denotes the distance from the compressed longitudinal bars centroid to the edge of columns; a_a denotes the distance from the tensile steel flange outer edge to the edge of columns; and a'_a denotes the distance from the compressed steel flange outer edge to the edge of columns.

4.4. Validation. According to the proposed formula above, the calculation bearing capacities of 54 columns with a slenderness ratio of 14 are presented in Table 3. Figure 19 depicts a comparison between the ultimate strengths obtained from the calculations and those derived from FEA. It can be observed that there is a significant error in the calculated results for specimens with an eccentricity of 0.8. The primary

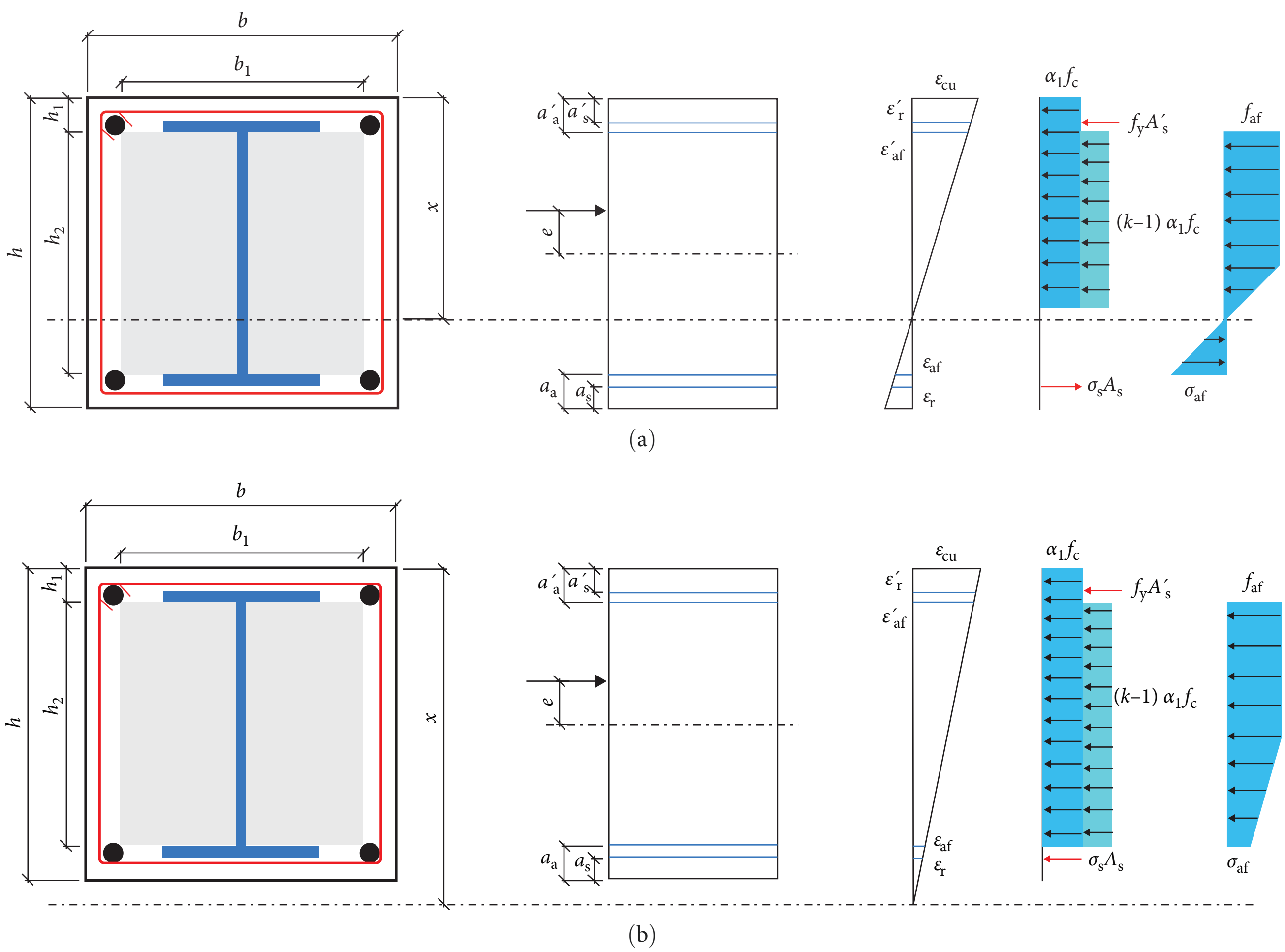

FIGURE 18: Stress–strain diagram of small eccentricity failure specimen: (a) $x_b < x \le h - a_a$; (b) $x > h - a_a$.

TABLE 3: Comparison between the calculated values (N_{cal}) and the numerical values (N_{num})

Specimens	f_{cu}/(N/mm^2)	f_{ys}/(N/mm^2)	$D \times t$ (mm)	α_s (%)	e/B	N_{num} (kN)	N_{cal} (kN)	N_{cal}/N_{num}
CSTRC-A-1	30	345	250 × 2	4	0.05	6,821.8	6,119.2	0.897
CSTRC-A-2	30	345	250 × 2	4	0.1	5,986.7	5,705.3	0.953
CSTRC-A-3	30	345	250 × 2	4	0.2	4,640.0	4,876.6	1.051
CSTRC-A-4	30	345	250 × 2	4	0.4	2,930.1	3,020.9	1.031
CSTRC-A-5	30	345	250 × 2	4	0.5	2,406.7	2,281.6	0.948
CSTRC-A-6	30	345	250 × 2	4	0.8	1,499.8	1,321.3	0.881
CSTRC-B-1	40	345	250 × 2	4	0.05	8,128.8	7,692.1	0.946
CSTRC-B-2	40	345	250 × 2	4	0.1	7,139.5	6,982.6	0.978
CSTRC-B-3	40	345	250 × 2	4	0.2	5,498.5	5,922.6	1.077
CSTRC-B-4	40	345	250 × 2	4	0.4	3,421.8	3,625.9	1.060
CSTRC-B-5	40	345	250 × 2	4	0.5	2,782.7	2,652.2	0.953
CSTRC-B-6	40	345	250 × 2	4	0.8	1,698.5	1,445.0	0.851
CSTRC-C-1	50	345	250 × 2	4	0.05	9,346.2	9,112.5	0.975
CSTRC-C-2	50	345	250 × 2	4	0.1	8,173.4	8,157.1	0.998
CSTRC-C-3	50	345	250 × 2	4	0.2	6,307.5	6,831.0	1.083
CSTRC-C-4	50	345	250 × 2	4	0.4	3,877.1	4,125.2	1.064
CSTRC-C-5	50	345	250 × 2	4	0.5	3,134.1	2,949.2	0.941
CSTRC-C-6	50	345	250 × 2	4	0.8	1,881.0	1,531.1	0.814
CSTRC-D-1	40	235	250 × 2	4	0.05	7,367.8	7,516.4	1.020

Table 3: Continued.

Specimens	f_{cu}/(N/mm^2)	f_{ys}/(N/mm^2)	$D\times t$ (mm)	α_s (%)	e/B	N_{num} (kN)	N_{cal} (kN)	N_{cal}/N_{num}
CSTRC-D-2	40	235	250 × 2	4	0.1	6,523.7	6,923.3	1.061
CSTRC-D-3	40	235	250 × 2	4	0.2	5,095.5	5,629.5	1.105
CSTRC-D-4	40	235	250 × 2	4	0.4	3,164.8	3,030.8	0.958
CSTRC-D-5	40	235	250 × 2	4	0.5	2,547.1	2,326.7	0.914
CSTRC-D-6	40	235	250 × 2	4	0.8	1,512.7	1,170.6	0.774
CSTRC-B-1	40	345	250 × 2	4	0.05	8,128.8	7,692.1	0.946
CSTRC-B-2	40	345	250 × 2	4	0.1	7,139.5	6,982.6	0.978
CSTRC-B-3	40	345	250 × 2	4	0.2	5,498.5	5922.6	1.077
CSTRC-B-4	40	345	250 × 2	4	0.4	3,421.8	3,625.9	1.060
CSTRC-B-5	40	345	250 × 2	4	0.5	2,782.7	2,652.2	0.953
CSTRC-B-6	40	345	250 × 2	4	0.8	1,698.5	1,445.0	0.851
CSTRC-E-1	40	420	250 × 2	4	0.05	8,595.8	7,759.3	0.903
CSTRC-E-2	40	420	250 × 2	4	0.1	7,487.9	7,020.3	0.938
CSTRC-E-3	40	420	250 × 2	4	0.2	5,753.7	6,106.2	1.061
CSTRC-E-4	40	420	250 × 2	4	0.4	3,560.1	3,742.3	1.051
CSTRC-E-5	40	420	250 × 2	4	0.5	2,912.7	2,834.1	0.973
CSTRC-E-6	40	420	250 × 2	4	0.8	1,805.1	1,607.0	0.890
CSTRC-B-1	40	345	250 × 2	4	0.05	8,128.8	7,692.1	0.946
CSTRC-B-2	40	345	250 × 2	4	0.1	7,139.5	6,982.6	0.978
CSTRC-B-3	40	345	250 × 2	4	0.2	5,498.5	5,922.6	1.077
CSTRC-B-4	40	345	250 × 2	4	0.4	3,421.8	3,625.9	1.060
CSTRC-B-5	40	345	250 × 2	4	0.5	2,782.7	2,652.2	0.953
CSTRC-B-6	40	345	250 × 2	4	0.8	1,698.5	1,445.0	0.851
CSTRC-F-1	40	345	250 × 3.01	6	0.05	9,037.6	8,529.1	0.944
CSTRC-F-2	40	345	250 × 3.01	6	0.1	7,932.3	8,100.4	1.021
CSTRC-F-3	40	345	250 × 3.01	6	0.2	6,106.5	6,722.2	1.101
CSTRC-F-4	40	345	250 × 3.01	6	0.4	3,842.1	4,137.7	1.077
CSTRC-F-5	40	345	250 × 3.01	6	0.5	3,162.4	3,097.9	0.980
CSTRC-F-6	40	345	250 × 3.01	6	0.8	1,983.0	1,805.7	0.911
CSTRC-G-1	40	345	250 × 4.03	8	0.05	9,932.0	9,288.4	0.935
CSTRC-G-2	40	345	250 × 4.03	8	0.1	8,698.2	9,093.7	1.045
CSTRC-G-3	40	345	250 × 4.03	8	0.2	6,687.0	7,508.4	1.123
CSTRC-G-4	40	345	250 × 4.03	8	0.4	4,242.7	4,627.6	1.091
CSTRC-G-5	40	345	250 × 4.03	8	0.5	3,521.4	3,501.4	0.994
CSTRC-G-6	40	345	250 × 4.03	8	0.8	2,248.0	2,125.0	0.945
			Average ratio value					0.982
			Coefficient variation					0.080

Note. The slenderness ratio of all specimens is 14.

reason for this is in the simplified calculations, the restraint of concrete by the steel tube is neglected, and only the restraint of concrete by the T-shaped steel is considered. Consequently, the strength of the concrete is lower than its actual strength. For columns subjected to large eccentric compression, the height of the compressed concrete zone is significantly lower than that in columns subjected to small eccentric compression. This leads to significant disparities between the calculated results and simulation outcomes for columns subjected to large eccentric compression. However, overall, the calculated values align well with the simulated values. The average ratio of calculate to numerical value is 0.982, with a coefficient variation of 0.08.

5. Conclusions

The mechanical performance of the CSTRC columns under eccentric compression is studied by the FEA model. The strain and stress distribution of the concrete section and the steel section are analyzed, and the influence of various parameters on the eccentric compression performance of the CSTRC column is discussed. Finally, a set of formulas for

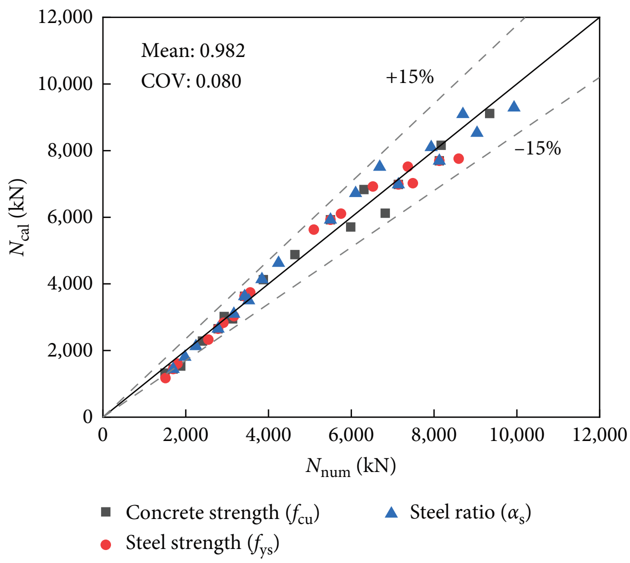

Figure 19: Comparison of the ultimate strengths obtained from the calculated and the FEA.

calculating the eccentric ultimate load value is proposed according to the plane section assumption. The conclusions are as follows:

(1) An effective finite element model is established to simulate the eccentric compression properties of the CSTRC column, and the load–displacement curves, load–strain curves, and ultimate load value obtained by the FEA model are in good agreement with the existing test results. The average ratio is 1.02, and the standard deviation is 0.05.
(2) When the eccentricity is 0.2, the specimen exhibits characteristics indicative of small eccentricity failure. Conversely, when the eccentricity is 0.8, the specimen demonstrates traits associated with large eccentricity failure. Furthermore, as the eccentricity increases, there is a notable decrease in the specimen's bearing capacity.
(3) The slenderness ratio will affect the failure mode of the CSTRC columns; when the slenderness ratio of specimens exceeds 22, the influence of the second-order effect should be considered. In addition, increasing the concrete strength, steel strength, and steel ratio can significantly enhance the ultimate load values of the CSTRC columns.
(4) A set of formulas for calculating the eccentric load values of CSTRC columns is proposed. The ultimate strength calculated by the proposed method is compared with the numerical results, and the results show that the calculated values are in good agreement with the numerical values.

In the current work, the study of the lateral compression performance of columns has been limited to finite element simulations. It is imperative to further investigate the load-bearing capacity and failure modes of columns under eccentric compression through experimental tests. Additionally, there is a need to intensify research on the design methods and construction processes of columns.

Data Availability

The data that support the findings of this study are available upon reasonable request from the corresponding author.

Conflicts of Interest

The authors declare that they have no conflicts of interest

Acknowledgments

This work is supported by the National Natural Science Foundation of China (grant number 52178159), the Doctor Foundation of Shandong Jianzhu University (grant number X21009Z), and the Scientific Research Plan Projects of Education Department of Shaanxi Provincial Government (grant number 23JY040).

References

[1] L.-H. Han, W. Li, and R. Bjorhovde, "Developments and advanced applications of concrete-filled steel tubular (CFST) structures: members," *Journal of Constructional Steel Research*, vol. 100, pp. 211–228, 2014.
[2] A. Fam, F. S. Qie, and S. Rizkalla, "Concrete-filled steel tubes subjected to axial compression and lateral cyclic loads," *Journal of Structural Engineering*, vol. 130, no. 4, pp. 631–640, 2004.
[3] E. Ellobody, B. Young, and D. Lam, "Behaviour of normal and high strength concrete-filled compact steel tube circular stub columns," *Journal of Constructional Steel Research*, vol. 62, no. 7, pp. 706–715, 2006.
[4] X.-S. Shi, Q.-Y. Wang, X.-L. Zhao, and F. G. Collins, "Structural behaviour of geopolymeric recycled concrete filled steel tubular columns under axial loading," *Construction and Building Materials*, vol. 81, pp. 187–197, 2015.
[5] Y.-Y. Lu, N. Li, S. Li, and H.-J. Liang, "Behavior of steel fiber reinforced concrete-filled steel tube columns under axial compression," *Construction and Building Materials*, vol. 95, pp. 74–85, 2015.
[6] W. Wang, X. Lyu, Y. Zhang, Y. Yu, and T. Zhang, "Axial compression performance of thin-walled T-shaped concrete filled steel tubular columns under constant high temperature: experimental and numerical study," *Structures*, vol. 27, pp. 525–541, 2020.
[7] X. Zhou, J. Liu, X. Wang, and Y. F. Chen, "Behavior and design of slender circular tubed-reinforced-concrete columns subjected to eccentric compression," *Engineering Structures*, vol. 124, pp. 17–28, 2016.
[8] M. Ahmed, Q. Q. Liang, V. I. Patel, and M. N. S. Hadi, "Behavior of eccentrically loaded double circular steel tubular short columns filled with concrete," *Engineering Structures*, vol. 201, pp. 109790–109790, 2019.
[9] C.-H. Lee, T. H.-K. Kang, S.-Y. Kim, and K. Kang, "Strain compatibility method for the design of short rectangular concrete-filled tube columns under eccentric axial loads," *Construction and Building Materials*, vol. 121, pp. 143–153, 2016.
[10] M. M. Hassan, H. M. Ramadan, M. Abdel-Mooty, and S. A. Mourad, "Seismic behavior of braced frames with

different connection details to concrete filled tube columns," *Structures*, vol. 28, pp. 2379–2391, 2020.

[11] D. A. Aguirre, M. J. Kowalsky, J. M. Nau, M. Gabr, and G. Lucier, "Seismic performance of reinforced concrete filled steel tube drilled shafts with inground plastic hinges," *Engineering Structures*, vol. 165, pp. 106–119, 2018.

[12] J.-P. Liu, Y.-L. Yang, H. Song, and Y.-Y. Wang, "Numerical analysis on seismic behaviors of T-shaped concrete-filled steel tubular columns with reinforcement stiffeners," *Advances in Structural Engineering*, vol. 21, no. 9, pp. 1273–1287, 2018.

[13] H.-T. Thai, B. Uy, M. Khan, Z. Tao, and F. Mashiri, "Numerical modelling of concrete-filled steel box columns incorporating high strength materials," *Journal of Constructional Steel Research*, vol. 102, pp. 256–265, 2014.

[14] Y.-F. Fang, M.-C. Chen, and H. Huang, "Square CFST columns under cyclic load and acid rain attack: experiments," *Steel and Composite Structures*, vol. 30, no. 2, pp. 171–183, 2006.

[15] G.-H. Yao, Y.-J. Li, and F.-Y. Miao, "Behavior of concrete-filled steel tube reinforced concrete columns subjected to axial compression," *Journal of Building Structures*, vol. 34, no. 5, pp. 114–121, 2013.

[16] Y. Liu, Z.-X. Guo, L.-P. Jia, and Q.-M. Chen, "Experimental study on axial compression performance and design method of core steel tube reinforced concrete short columns," *Journal of Building Structures*, vol. 36, no. 12, pp. 135–142, 2015.

[17] J.-H. Zhao, Y.-L. Hou, and C.-G. Zhang, "Ultimate bearing capacity of square steel tube-reinforced high strength concrete column under axial compression," *Journal of Civil and Environmental Engineering*, vol. 38, no. 5, pp. 20–26, 2016.

[18] Y. Huang, D. Huang, G.-R. Chen, Y. Yang, and B. Peng, "Seismic performance limit states of steel tube-reinforced concrete columns," *Earthquake Engineering and Engineering*, vol. 38, no. 2, pp. 157–167, 2018.

[19] H.-X. Kang and J.-R. Qian, "Experimental study on axial compressive capacity of high strength concrete-filled steel tube composite columns," *Building Structure*, vol. 41, no. 6, pp. 64–67, 2011.

[20] J.-G. Nie, Y. Bai, and C.-S. Cai, "New connection system for confined concrete columns and beams I: experimental study," *Journal of Structural Engineering*, vol. 134, no. 12, pp. 1787–1799, 2008.

[21] J.-R. Qian and H.-X. Kang, "Experimental study on seismic behavior of high-strength concrete-filled steel tube composite columns," *Journal of Building Structures*, vol. 30, no. 4, pp. 85–93, 2009.

[22] X. Ji, M. Zhang, H. Kang, J. Qian, and H. Hu, "Effect of cumulative seismic damage to steel tube-reinforced concrete composite columns," *Earthquakes and Structures*, vol. 7, no. 2, pp. 179–199, 2014.

[23] J.-M. Cai, J.-L. Pan, and H. Su, "Experimental and analytical research on seismic behavior of ECC-encased concrete-filled steel tubular columns," *Journal of Building Structures*, vol. 41, no. 7, pp. 55–62, 2020.

[24] Y. Zhang, J. R. Qian, X. D. Ji, and W. L. Cao, "Tests and numerical simulation on short composite-sectioned concrete filled steel tubular columns subjected to axial compressive loading," *Advanced Materials Research*, vol. 374-377, pp. 2265–2270, 2011.

[25] Y.-F. Xu, G.-L. Jiang, C.-Y. Xiang, F. Hei, Z.-C. Chen, and X.-D. Ma, "Capacity study under axial load of circular steel tube compile short column filled with steel reinforced concrete," *Journal of Shenyang Jianzhu University*, vol. 21, no. 6, pp. 640–643, 2005.

[26] Y. Dai, J.-H. Zhao, and C.-G. Zhang, "Analysis of axial compression bearing capacity of CFRP and angel steel composite reinforced concrete-filled steel tubular columns," *Building Structure*, vol. 48, no. 17, pp. 101–108, 2018.

[27] Y. Yang, Y.-L. Yu, X.-L. Wang, K. An, and Y.-F. Pan, "Experimental study of seismic performance of composite columns with core steel tube and confined by prestressed steel strips," *Industrial Construction*, vol. 45, no. 3, pp. 11–15, 2015.

[28] P. Wang, X. You, Y. Tao, Q. Shi, and Q. Wang, "Axial compression behavior of core-steel tube with T-shaped flanges reinforced concrete column," *Journal of Constructional Steel Research*, vol. 198, Article ID 107586, 2022.

[29] D. Yaozong, *Study on seismic performace of new type steel reinforecd concrete columns*, M. S. thesis, Xi'an University of Architecture & Technology, Xian, China, 2021.

[30] B. Wang, *Research on eccentric compression experiment and load-bearing capacity calulation of steel tube-reinforced concrete column*, M. S. thesis, Taiyuan University of Technology, Shanxi, China, 2011.

[31] X.-Z. Zhao and F.-P. Wen, "Theoretical study on confinement mechanism and stress–strain model for steel confined concrete in SRC columns," *Engineering Mechanics*, vol. 35, no. 5, pp. 45–55, 2018.

[32] L.-H. Han and Y.-F. An, "Performance of concrete-encased CFST stub columns under axial compression," *Journal of Constructional Steel Research*, vol. 93, pp. 62–76, 2014.

[33] GB50010-2010, *Code for Design of Concrete Structures*, China Architecture & Building Press, Beijing, 2015.

[34] H. Yuan, H.-P. Hong, H. Deng, and Y. Bai, "Displacement ductility of staged construction-steel tube-reinforced concrete columns," *Construction and Building Materials*, vol. 188, pp. 1137–1148, 2018.

[35] Q. Wang, L. Liang, E. M. Lui, and Q. Shi, "Behavior of eccentrically loaded UHPC filled circular steel tubular short columns," *Journal of Constructional Steel Research*, vol. 193, Article ID 107282, 2022.

[36] Eurocode 2, "Design of concrete structures-part 1-1: general rules and rules for buildings," BS EN 1992-1-1: 2004, European Committee for Standardization, 2004.

[37] JGJ138-2016, *Code for Design Of Composite Structures*, China Architecture & Building Press, Beijing, 2016.